# Two-band Bose-Hubbard model for many-body resonant tunneling in the Wannier-Stark system

Carlos A. Parra-Murillo,[1] Javier Madroñero,[2] and Sandro Wimberger[1]

[1]*Institut für Theoretische Physik and Center for Quantum Dynamics, Universität Heidelberg, 69120 Heidelberg, Germany*
[2]*Departamento de Física, Universidad del Valle, Cali, Colombia*

We study an experimentally realizable paradigm of complex many-body quantum systems, a two-band Wannier-Stark model, for which diffusion in Hilbert space as well as many-body Landau-Zener processes can be engineered. A crossover between regular and quantum chaotic spectra is found within the many-body avoided crossings at resonant tunneling conditions. The spectral properties are shown to determine the evolution of states across a cascade of Landau-Zener events. We apply the obtained spectral information to study the nonequilibrium dynamics of our many-body system in different parameter regimes.

## I. INTRODUCTION

The rapid development of high-precision techniques for the experimental control of ultracold quantum gases offers a clean way to study static and dynamical properties of interacting many-body lattice systems [1–3]. Of particular interest are realizations of strongly correlated or complex quantum systems composed of many particles. Experiments controlling the populations of higher orbitals and bands in periodic potentials are now at hand [4,5]. This facilitates the study of many degree-of-freedom systems. Moreover, many-body quantum quenches, nonequilibrium dynamics, and real-time controlled sweep dynamics can be realized in the experiments [6–9]. This offers very good advantages for a better understanding of the underlying diffusion processes taking place not only in real space, but, more generally, in the Hilbert space [10–12]. In this latter context, aspects of integrability of quantum systems are crucial for predictions on, for instance, their relaxation dynamics and further thermalization [13–20].

In this paper, we present a case study of a complex many-body system including two strongly coupled energy bands. As we sketch in Sec. II A and in the Appendix, this can, for instance, be realized experimentally with ultracold bosons in accelerated (or equivalently tilted) optical lattices [21–23]. Our system represents a paradigm for the many-body physics in which the dynamics can be steered by the parameters (tilt, interaction strength, and potential depth), thus, implementing very different dynamics. Although the mean-field transport (weakly interacting limit) and the single-particle limit are well studied for one-dimensional Wannier-Stark systems [21,22,24,25], even the simplest many-body version, a one-band Bose-Hubbard model with(out) tilt, allows one to tune between regular and quantum chaotic evolutions [26–31]. In our problem, depending on the choice of parameters, full complexity in the interband transport in Hilbert space can be reached by sweeping predetermined initial states over resonant tunneling regions. This is possible since the strongest interband coupling occurs at resonantly enhanced tunneling (RET) between energy bands [24,25,32,33]. At resonant conditions, we find a clear crossover from regular to quantum chaotic spectral statistics as a function of a few system parameters. The complexity in the energy spectrum determines the transport across the many avoided crossings (ACs) at RET when the force becomes time dependent.

This not only generalizes results on the weakly interacting limit [34,35], but relates to the largely open problem of many-body Landau-Zener (LZ) processes in the presence of strong particle interactions [11,29,36]. As direct applications, we show how the spectral properties influence the diffusion in Hilbert space. We characterize different realistic scenarios for which relaxation toward equilibrium and spectral localization, on one hand, and diffusion, on the other hand, take place. This is performed with the help of controlled sweeps through the interband many-body resonant regimes.

This paper is organized as follows: In Sec. II, we introduce our two-band Bose-Hubbard model and the numerical methods implemented for the diagonalization. Its spectral properties are presented in Sec. III where the conditions for the emergence of chaos are discussed along with predictions for the dynamics. In Sec. IV, we study the diffusion processes for different spectra and initial conditions when driving the system through the resonant regime. Finally, Sec. V concludes the paper with a discussion of experimental ramifications.

## II. MANY-BODY WANNIER-STARK PROBLEM

### A. The two-band model

Our Wannier-Stark system consists of ultracold bosonic atoms in a one-dimensional optical lattice. An additional Stark force stimulates the quantum transport along the lattice [21–23,28] and, at the same time, couples the two lowest Bloch bands. The system we have in mind, see Eq. (1), could be realized experimentally with ultracold bosons in a doubly periodic optical lattice. For a convenient choice of the parameters, a well-isolated two-band system can be engineered, thus, neglecting the effects of the third and higher excited Bloch bands (see Fig. 9 in the Appendix). Further details on the realization can be found in the Appendix.

The corresponding many-particle problem can be described in the tight-binding (TB) limit by a two-band Bose-Hubbard Hamiltonian,

$$\hat{H} = \sum_{\beta=a,b} \hat{H}_\beta + \hat{H}_1 + \hat{H}_2, \tag{1}$$

with the terms in Eq. (1) defined by

$$\hat{H}_\beta = \sum_{l=1}^{L} -\frac{J_\beta}{2}(\hat{\beta}_{l+1}^\dagger \hat{\beta}_l + \text{H.c.}) + \frac{W_\beta}{2}\hat{\beta}_l^{\dagger 2}\hat{\beta}_l^2 + \varepsilon_l^\beta \hat{n}_l^\beta,$$

$$\hat{H}_1 = \sum_{l=1}^{L}\sum_\mu \omega_B C_\mu (\hat{a}_{l+\mu}^\dagger \hat{b}_l + \text{H.c.}), \qquad (2)$$

$$\hat{H}_2 = \sum_{l=1}^{L} 2W_x \hat{n}_l^a \hat{n}_l^b + \frac{W_x}{2}(\hat{b}_l^\dagger \hat{b}_l^\dagger \hat{a}_l \hat{a}_l + \text{H.c.}).$$

The bosonic annihilation (creation) operators at the $l$th site are $\hat{\beta}_l(\hat{\beta}_l^\dagger)$, and the number operators are $\hat{n}_l^\beta = \hat{\beta}_l^\dagger \hat{\beta}_l$. $\beta$ is the band index, i.e., $\beta = a$ for the lower band and $\beta = b$ for the upper one. The on-site energies are given by $\varepsilon_l^\beta = \omega_B l + \Delta_g \delta_{\beta,b}$, the Bloch frequency is $\omega_B = 2\pi F$, and $\Delta_g$ is the energy separation between the Bloch bands. $J_\beta$ are the hopping amplitudes. The on-site interparticle interaction in the bands is assumed to be repulsive with strength $W_\beta > 0$. The coupling between the bands is given by: (i) the *dipolelike* terms in $\hat{H}_1$ with strength proportional to $C_\mu$, where the integer index $\mu$ is symmetric around 0 and (ii) the interaction terms with strength $W_x$ in $\hat{H}_2$.

In the single-particle picture, the interband coupling is maximal at specific tilts $F_r \approx \Delta_g/2\pi r$. At those values, RET occurs between levels located at wells separated by a distance $r$. This integer $r = l_a - l_b$ is called the order of the resonance [24]. The above resonance formula is modified to

$$F_r = \Delta_g/2\pi\sqrt{r^2 - 4C_0^2}, \qquad (3)$$

by taking into account the Stark shift of the levels [34].

### B. The Floquet-Bloch operator and its numerical diagonalization

It is convenient to transform the Hamiltonian (1) into the interaction picture with respect to the external force, which removes the tilt $\sum_{l,\beta} \omega_B l \hat{n}_l^\beta$ and transforms the hopping terms as $\hat{\beta}_{l+1}^\dagger \hat{\beta}_l \to \hat{\beta}_{l+1}^\dagger \hat{\beta}_l \exp(-i\omega_B t)$. In addition, in this procedure, the dipolelike couplings with $|\mu| > 0$ are transformed as $\hat{a}_{l+\mu}^\dagger \hat{b}_l \to \hat{a}_{l+\mu}^\dagger \hat{b}_l \exp(-i\omega_B \mu F t)$. The gauge-transformed Hamiltonian is now translationally invariant and time dependent with the fundamental period $T_B = 2\pi/\omega_B$, the Bloch period, i.e., $\hat{H}(t + T_B) = \hat{H}(t)$. This condition holds because the remaining frequencies are integer multiples of $\omega_B$. We are now allowed to impose periodic boundary conditions in space, i.e., by identifying $\hat{\beta}_{L+1}^\dagger = \hat{\beta}_1^\dagger$. Therefore, a suitable basis for numerical diagonalization is given by the translationally invariant Fock states $\{|\gamma\rangle\}$ defined in Refs. [28–30]. We can also work with the Floquet Hamiltonian $\hat{H}_f = \hat{H}(t) - i\partial_t$ [37] for which the eigenvalue equation reads

$$\varepsilon_i \hat{1}|\phi_{\varepsilon_i}^k\rangle = (\hat{H}_0 - \omega_B k\hat{1})|\phi_{\varepsilon_i}^k\rangle + \hat{J}|\phi_{\varepsilon_i}^{k-1}\rangle + \hat{J}^\dagger|\phi_{\varepsilon_i}^{k+1}\rangle$$

$$+ \sum_\mu \left[\hat{C}_\mu|\phi_{\varepsilon_i}^{k-\mu}\rangle + \hat{C}_\mu^\dagger|\phi_{\varepsilon_i}^{k+\mu}\rangle\right]. \qquad (4)$$

Here we used multimode Fourier decomposition of the eigenstates of $\hat{H}_f$ [38], i.e., $|\phi_n(t)\rangle = \sum_k \exp(-ik\omega_B t)|\phi_{\varepsilon_n}^k\rangle$ with $k = k_1 + 2k_2 + \cdots + \mu k_\mu$. The operator $\hat{H}_0$ contains all the time-independent terms of the gauge-transformed Hamiltonian $\hat{H}(t)$, and the operators $\hat{J}$ and $\hat{C}_\mu$ are defined by the hopping and dipolelike transition terms $\hat{J} = -\sum_{l,\beta} J_\beta \hat{\beta}_{l+1}^\dagger \hat{\beta}_l/2$ and $\hat{C}_\mu = \omega_B C_\mu \sum_l a_{l+\mu}^\dagger b_l$, respectively. In order to diagonalize (4), we use the expansion $|\phi_n^k\rangle = \sum_k A_{k,\gamma}|\gamma\rangle$, which implies that the Floquet operator is represented by a block matrix. Since $|C_\mu|$ drops faster to zero as $|\mu|$ increases because of the decreasing overlapping between the Wannier states at different lattice sites, we can neglect all processes with $C_{|\mu|>r}$. In this paper, we restrict to resonances of orders $r = 1$ and $r = 2$, then, the Floquet matrix is reduced to a five-block diagonal matrix (see Appendix 2 [10]) with every block size given by the dimension of the Hamiltonian (1).

In order to compute the quasienergies $\varepsilon_i$ (eigenvalues of $\hat{H}_f$), we numerically diagonalized Eq. (4) by a Lanczos algorithm [39]. The quasienergies lie within the so-called Floquet zone (FZ): $\varepsilon_i \in [\varepsilon_0 - \omega_B/2, \varepsilon_0 + \omega_B/2]$ of width $\omega_B$ and centered at $\varepsilon_0$. We conveniently set $\varepsilon_0$ as a function of $F$ in order to improve the visualization of the spectrum in the different regions of interest. Due to the periodicity of the quasienergies, the extended spectrum is given by the operation $\varepsilon_i \to \varepsilon_i + n_{fz}\omega_B$ with the index $n_{fz}$ of the FZ. For $N$ atoms distributed in $L$ lattice sites, the number of quasienergies is given by $\mathcal{N}_s = (N + 2L - 1)!/[LN!(2L - 1)!]$, considering the reduction by a factor $L$ arising from the translational symmetry [28–30]. However, the effective dimension of $\hat{H}_f$ in Eq. (4) is much larger: $\mathcal{N}_s \Delta k$, with $\Delta k = 10 \cdots 50$ being the number of Floquet components needed to obtain a number $\mathcal{N}_s$ of convergent eigenstates. This latter procedure is equivalent to diagonalizing the evolution operator integrated over one Bloch period $\hat{U}_{T_B} = \hat{T} \exp[-i\int_0^{T_B} \hat{H}(t)dt]$, where $\hat{T}$ is the time-ordering operator. Nevertheless, the diagonalization of $\hat{H}_f$ has advantages with respect to the computation times for larger systems and large $T_B$.

### III. SPECTRAL PROPERTIES OF THE TWO-BAND WANNIER-STARK SYSTEM

#### A. The single-particle limit and the two-band manifold approach

Let the force $F$ be the control parameter to analyze the spectrum in the plane $\varepsilon$-$F$ as shown in Fig. 1(a) for the single-particle case. The gap $\Delta_g$, typically the largest energy scale in Eq. (1) for experimental realization (see the Appendix), allows us to split up the spectrum into equidistant subsets of states, each labeled by the upper band occupation number,

$$M \equiv \langle\varepsilon_i| \sum_l \hat{n}_l^b |\varepsilon_i\rangle. \qquad (5)$$

In the off-resonant regime where $F$ is not close to $F_r$, $M$ is a good quantum number since the eigenstates of $\hat{H}_f$ essentially correspond to specific basis states, i.e., to translationally invariant Fock states $|\gamma\rangle$. One can group these states into $N + 1$ subsets of states with the same $M$ and dimension
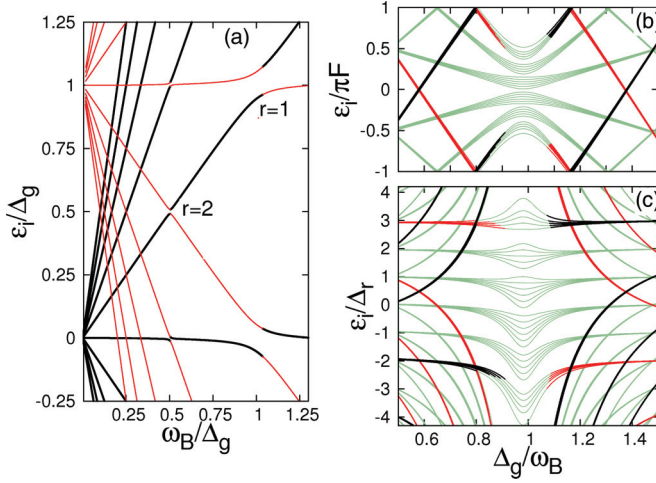
FIG. 1. (Color online) The spectrum vs Stark force $F$: (a) two-band Wannier-Stark ladders for the single-particle case for $\Delta_g = 0.796$ (corresponding to lattice parameters $V_0 = 5$ and $z_0 = 2.5$, see the Appendix). Avoided crossings appear at the resonances $F_r$ with width $\Delta_r^{\min} \ll \Delta_g$. (b) and (c) The many-body spectrum for $N/L = 5/3$ with no interparticle interaction, revealing the presence of the $M$ manifolds discussed in Sec. III. The different lines correspond to eigenstates of the type: lower-band-like states $\{|N\rangle_a \otimes |0\rangle_b\}$ (black lines), upper-band-like states $\{|0\rangle_a \otimes |N\rangle_b\}$ (thick red lines), and mixedlike states $\{|N - M\rangle_a \otimes |M\rangle_b\}$ (thin green lines). The remaining parameters are $C_0 = -0.095, C_1 = 0.04, C_2 = 0.004, J_a = 0.078,$ and $J_b = -0.24$.

$$\mathcal{N}_M = \frac{1}{L}\binom{M+L-1}{L-1}\binom{N-M+L-1}{L-1} < \mathcal{N}_s.$$ Hereafter, we refer to those subsets as $M$ manifolds.

In the noninteracting case, i.e., $W_{a,b,x} = 0$, the internal manifold states are degenerate as shown by the level bunching in Figs. 1(b) and 1(c). The simplest case is that for $F = 0$ for which the commutator $[\hat{H}, \hat{M}] = 0$. Then the Hamiltonian factorizes into a block matrix $\hat{H} = \bigoplus_{M=0}^{N} \hat{\mathcal{H}}_M$. Note that the blocks $\hat{\mathcal{H}}_0$ and $\hat{\mathcal{H}}_N$ correspond to the independent Bose-Hubbard Hamiltonians $\hat{H}_{\beta=a,b}$, respectively. Therefore, we can think of the Hamiltonian in (1) as two tilted Bose-Hubbard chains, connected through the midmanifolds $0 < M < N$ when $F \neq 0$. The central manifolds contain all information about the interband coupling since they correspond to mixtures between states from both bands, for instance, Fock states of type $|\vec{n}_{a,b}\rangle \leftrightarrow |N - M\rangle_a \otimes |M\rangle_b$. Furthermore, there is no direct coupling term between the blocks $\hat{\mathcal{H}}_0$ and $\hat{\mathcal{H}}_N$. The interband coupling can be understood as the mixing of the $N + 1$ manifolds, which is mainly induced by the one- and two-particle exchange terms in (2), that is, $\hat{H}_1(F \neq 0)$ and $\hat{H}_2(W_x \neq 0)$.

Around the RET of order $r$, see Eq. (3), the Hamiltonian (1) can effectively be transformed into a resonant Hamiltonian $\hat{H}_r$ by setting the reference system as $l_a = 0$ with $l_b = -r$. Additionally, we define the manifold projectors,

$$\hat{P}_M = \sum_i |\vec{n}_{a,b}, M\rangle_i \,_i\langle \vec{n}_{a,b}, M|, \tag{6}$$

where $|\vec{n}_{a,b}, M\rangle \equiv |n_1^a, n_2^a, \ldots\rangle \otimes |n_1^b, n_2^b, \ldots\rangle$. The closure condition is given by $\sum_M \hat{P}_M = 1$. This allows one to
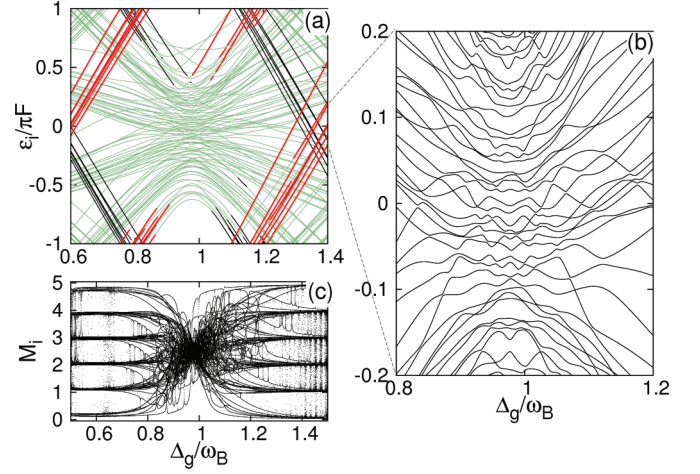


FIG. 2. (Color online) Interaction effects: (a) interacting many-body spectra for $N/L = 5/3$ [see Fig. 1(a)]. (b) Zoom around the resonance position revealing the emerging cluster of avoided crossings. (c) Manifold number $M_i$ for all Floquet eigenstates as a function of the ratio $\Delta_g/\omega_B$. Here the manifold structure is clearly seen before and after the single-particle resonance $F_{r=1} = 0.128$, characterized by the bunches of eigenstates with approximately the same upper band occupation number $M$. The parameters are the same as those in Fig. 1 with additional interaction strengths $W_a = 0.023, W_b = 0.027,$ and $W_x = 0.025$ [see Eq. (2)].

transform the Schrödinger equation $\hat{H}_r|\psi\rangle = E|\psi\rangle$ into the $M$ representation where the resonant Hamiltonian becomes

$$\hat{H}_r \simeq \sum_{M=0}^{N} \varepsilon_M^r |\psi_M\rangle\langle\psi_M| + \tilde{\omega}_B(|\psi_M\rangle\langle\psi_M + 1| + \text{H.c.}). \tag{7}$$

Here $\varepsilon_M^r = (\Delta_g - \omega_B r)M + (J_a - J_b)M, \tilde{\omega}_B \equiv \omega_B C_0$ $\sqrt{M + 1}, |\psi_M\rangle = \hat{P}_M|\psi\rangle$, and we used $N = N_a + N_b$ with $M \equiv N_b$. In this expression for $\varepsilon_M^r$, the order of the resonance (cf. Sec. II A) is approximated by $r \approx \Delta_g/\omega_B$. For typical parameters, we have that $\Delta_g, \omega_B \gg |J_b - J_a|$. Note that we disregard the dipolelike processes $|C_{|\mu|\geqslant 1}|$, which are only relevant at the exact resonance inducing a splitting of the manifold levels. In this representation, the Hamiltonian is clearly transformed into a TB-type Hamiltonian for the manifolds where the first-neighbor interaction is induced by a one-particle exchange with transition strength proportional to $\omega_B C_0$. Therefore, certain localization features are expected in energy space (as discussed in other contexts in Refs. [12,40]), which, in our case, imply a high occupation probability of a specific $M$ manifold.

An important energy scale is given by the energy difference between neighboring manifolds $|\psi_M\rangle$ and $|\psi_M + 1\rangle$, which characterizes the one-particle exchange process [see Fig. 2(c)]. This scale can be estimated by diagonalizing the $2 \times 2$ Hamiltonian matrix,

$$H_{2\times 2} = \begin{pmatrix} \varepsilon_{M+1}^r & \omega_B C_0 \\ \omega_B C_0 & \varepsilon_M^r \end{pmatrix}, \tag{8}$$

from which we obtain

$$\Delta_r = \Delta_g \sqrt{(1 - \omega_B r/\Delta_g)^2 + 4(\omega_B C_0/\Delta_g)^2}. \tag{9}$$
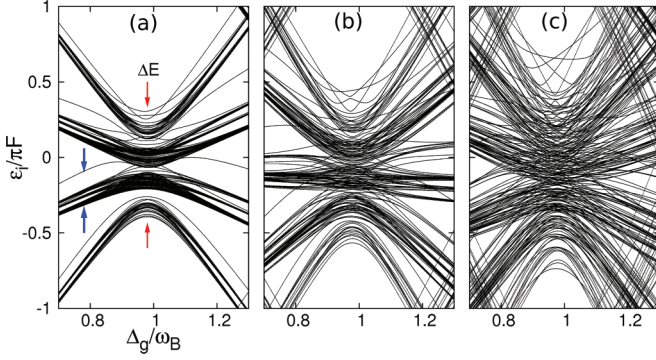
FIG. 3. (Color online) Manifold mixing: interacting many-body spectra as a function of the filling factor: (a) $N/L = 3/13$, (b) $N/L = 4/5$, and (c) $N/L = 5/4$. Strong manifold mixing occurs as $N/L$ increases due to the high density of avoided crossings in the resonant regime. The arrows in (a) represent: the (red, thin) width of the many-body avoided crossing $\Delta E$ and (blue, thick) the maximal energy splitting of the central manifold $M = 1$. The parameters are the same as those in Fig. 2.

The minimal width of the bow-tie-shaped many-body noninteracting spectrum in Fig. 1(b) is, thus, straightforwardly given by $\Delta E = N\Delta_r^{\min}$ with $\Delta_r^{\min} = 2\omega_B|C_0|$.

## B. Interaction effects and manifold mixing at resonant tunneling

The interparticle interaction $(W_{a,b,x} \neq 0)$ splits up the internal manifold levels, and strong level mixing occurs at the RET condition when the levels come closest. Then ACs appear due to the level repulsion, which arises from the lack of symmetries [see Fig. 2(b)]. The number of ACs is the larger, the larger the filling factor $N/L$ (see Fig. 3). The maximal splittings by the on-site interparticle interaction occur due to those states with $M$ particles occupying a single-particle level in one lattice site [see blue arrows in Fig. 3(a)], for example, $|N - M, 0, \ldots\rangle_a \otimes |M, 0, \ldots\rangle_b$. These are given by

$$\left(U_a^M\right)_{\max} = \frac{W_a}{2}(N - M)(N - M - 1),$$

$$\left(U_b^M\right)_{\max} = \frac{W_b}{2}M(M - 1), \qquad (10)$$

$$\left(U_{ab}^M\right)_{\max} = 2W_x(N - M)M.$$

With these quantities, we can compute the maximal manifold splitting as $U(M) \equiv \max\{(U_{\beta=a,b}^M)_{\max}, (U_{ab}^M)_{\max}\}$. Then we estimate the width $\Delta E$ of the many-body avoided crossing as

$$\Delta E = N\Delta_r^{\min} + U(N) = N\Delta_r^{\min} + \frac{W_b}{2}N(N - 1). \quad (11)$$

This follows from the fact that the maximal splitting is generated by those states with total particle number $N$ in one lattice site in the upper Bloch band $\beta = b$. Both scales $U(M = 1)$ and $\Delta E$ are sketched by the two pairs of arrows in Fig. 3(a).

The mixing in the spectrum is the strongest, the closer the central manifolds are, namely, around $F_r$. Therefore, there are neither characteristic energy scales nor good quantum numbers. Conversely, in the off-resonant regime, the energy

spectrum is characterized not only by the manifold number $M$, but also by the numbers $\theta_\beta = \langle \varepsilon_i | \sum_l \hat{n}_l^\beta (\hat{n}_l^\beta - 1)/2 | \varepsilon_i \rangle$ and $\theta_x = 2\langle \varepsilon_i | \sum_l \hat{n}_l^a \hat{n}_l^b | \varepsilon_i \rangle$. The latter numbers arise from the energy splitting induced by the interaction terms in Eq. (2). In this way, the eigenenergies can be approached by

$$\varepsilon_i(M, \vec{\theta}) \approx M_i \Delta_r + W_a \theta_{a,i} + W_b \theta_{b,i} + W_x \mu_{x,i}. \qquad (12)$$

The effective region of manifold mixing, the RET regime, is that for which the cluster of ACs is visible. Therein, $M$, $\theta_\beta$, and $\theta_x$ are no longer good quantum numbers since even the identification of the otherwise most distant manifolds $M = 0$ and $M = N$ becomes difficult. Manifold mixing is a local effect whenever $\Delta_g \gg J_\beta, W_{a,b,x}, C_s$ and $\Delta_g \approx r\omega_B$. Nevertheless, global mixing can be engineered, for instance, by decreasing the energy band gap to a value comparable with the interaction strengths, i.e., $\Delta_g \approx W_{a,b,x}$. Global mixing in the energy spectrum implies the destruction of the local resonances at $F = F_r$. Therefore, resonant tunneling generated by the interparticle interaction $W_{a,b}$ [6,7] has the same relevance as the one generated by the interband coupling terms $C_\mu$ and $W_x$.

In both cases, local or global manifold mixing, the spectral properties of (1) can be very complicated. Nevertheless, it is still possible to characterize the many-body spectrum in terms of the following subset of parameters: $(g, N/L, \Delta_g)$. Here $g$ is a prefactor that controls the strength of the interparticle interaction defined as $W_{a,b,x} \to gW_{a,b,x}$. Experimentally, changing $g$ is realized by varying the two-body scattering length via Feshbach resonances [2,7].

We now rescale the Hamiltonian (1) by the energy gap and then compute its commutator with the manifold number operator $\hat{M}$. This results in

$$[\hat{H}/\Delta_g, \hat{M}] = \frac{1}{\Delta_g}([\hat{H}_1, \hat{M}] + [\hat{H}_2, \hat{M}])$$

$$= \frac{\omega_B}{\Delta_g} \sum_{l,\mu} C_\mu(\hat{a}_{l+\mu}^\dagger \hat{b}_l - \text{H.c.}) \qquad (13)$$

$$- \frac{gW_x}{2\Delta_g} \sum_l (\hat{b}_l^\dagger \hat{b}_l^\dagger \hat{a}_l \hat{a}_l - \text{H.c.}).$$

From this equation, we see that one- and two-particle exchange operators, corresponding to the two interband coupling processes, are mainly responsible for the mixing properties. Let us now fix the force to $F = F_r$ for which the interband coupling is maximized. Then we vary the filling factor, the band gap, and the strength of the interparticle interaction. We have various cases:

(i) At resonance, we have $\omega_B/\Delta_g \approx 1/r$. If $g = 1$, this implies that, for high-order resonances $(r > 2)$, $\hat{H}_2$ dominates only if $\Delta_g \lesssim W_x$, otherwise, the band coupling is weak and the commutator (11) goes to zero.

(ii) For $r = 1$ and $\Delta_g \gg W_x$, $\hat{H}_1$ dominates, i.e., $\Delta_r$ is approximately a good energy scale. If $\Delta_g \sim W_x$, both $\hat{H}_1$ and $\hat{H}_2$ are equally important.

(iii) At condition (ii) with $\Delta_g \sim W_x$, the filling factor plays an important role. In the case of $N/L \ll 1$, we are close to the single-particle limit, which is nearly integrable. As the filling factor increases, so does the number of Fock states with double occupancies in a single lattice site, therefore, there is
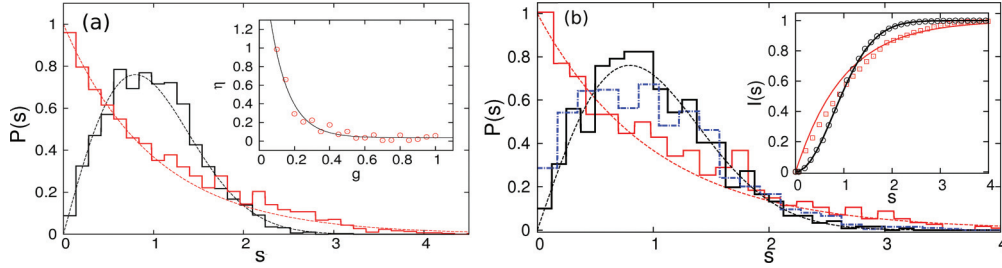
FIG. 4. (Color online) Regular-to-chaotic transition: (a) The main panel shows the level spacing distribution $P(s)$ for $N/L = 7/5$ ($\mathcal{N}_s = 2288$) for the interparticle control parameter (Sec. III) $g = 0.1$ (red, gray histogram, $\eta = 0.98$) and $g = 1.0$ (black histogram, $\eta = 0.056$), and $W_x = W_a = W_b = 0.025$. The inset shows the parameter $\eta$ as a function of $g$ where the black line corresponds to an exponential fit. (b) The main panel depicts the level spacing distribution $P(s)$ for three different filling factors: $N/L = 3/25$ ($\mathcal{N}_s = 848$, red, gray histogram), $N/L = 4/11$ ($\mathcal{N}_s = 1050$, blue dashed-dotted histogram), and $N/L = 6/5$ ($\mathcal{N}_s = 1001$, black thick histogram). The random-matrix theory (RMT) distributions are those in dashed lines in both panels. The inset shows the cumulative distribution $I(s)$ for the systems: $N/L = 3/25$ (red, gray $\square$) and $N/L = 6/5$ (black $\circ$). The solid lines represent the RMT prediction for $I(s)$ Poisson (red, gray) and GOE (black). The other parameters are the same as in the previous figures.

a strong interplay between one- and two-particle exchanges. This naturally induces an enhancement of the manifold mixing.

In terms of the $M$ manifolds, to consider the two-particle exchange process introduces a second-neighbor transition term in our tight-binding Hamiltonian of Eq. (7). Such types of extended TB-type Hamiltonians are usually nonintegrable (see Refs. [17,18] and references therein). We conclude that the many-body spectrum is strongly mixed when $\hat{H}_1$ and $\hat{H}_2$ have the same relevance, i.e., for the conditions $|C_0|/r \sim W_x/2\Delta_g$ and $N/L \sim 1$. The latter can be achieved in both local, i.e., at RET, and global, i.e., for $\Delta_g \approx W_{a,b,x}$ manifold mixings.

### C. Emergence of many-body quantum chaos

We now investigate the many-body spectra by means of random-matrix measures [41]. We study the level spacing (or local gap) distribution $P(s_i)$ with $s_i = \varepsilon_{i+1} - \varepsilon_i$, where $\langle s_i \rangle = 1$ after an appropriated unfolding procedure [10,41]. The crossover between regular (Poisson) $P_P(s) = \exp(-s)$ and quantum chaotic [Wigner-Dyson or Gaussian orthogonal ensemble (GOE)] statistics $P_W(s) = \pi s \exp(-\pi s^2/4)/2$ can be reached in several ways.

First, for an energy band gap $\Delta_g \lesssim 1$, we found that all systems with $N/L \sim 1$ are fully chaotic as shown in the main panel of Fig. 4(a) for $N/L = 7/5$. This is expected according to the commutator (13) and its respective discussion in the previous subsection.

Second, for fixed filling factor $N/L \sim 1$, quantum chaos can be tuned by the prefactor $g$ of the interparticle interaction terms. In order to check this crossover, we compute the parameter,

$$\eta = \frac{\int_0^{s_0} [P(s) - P_W(s)]ds}{\int_0^{s_0} [P_P(s) - P_W(s)]ds}, \tag{14}$$

where $s_0 = 0.4729 \cdots$ is the intersection point between the distributions $P_P(s)$ and $P_W(s)$. $\eta$ is plotted as a function of $g$ in the inset of Fig. 4(a). Herein, $\eta = 1$ for a perfect Poissonian distribution, and $\eta = 0$ for a perfect Wigner-Dyson distribution.

Deviations from the limiting random-matrix distributions are found for filling factors approaching the single-particle

limit for $N/L \ll 1$. This is seen in Fig. 4(b) for $N/L = 3/25$ and $N/L = 4/11$.

Due to the high dimensional parameter space of our system, perfect Poissonian distributions are not easy to find at the RET domain. On the other hand, good chaotic distributions are straightforwardly obtained. This is shown in the inset of Fig. 4(b) where the respective cumulative distribution is plotted, that is, $I(s) = \int_0^s P(s')ds'$. For the remaining combinations of parameters, we always obtain deviations characterized by nonfully chaotic level spacing distributions [10]. $N/L \sim 1$ and $|C_0| \sim W_x/2\Delta_g$ are similar conditions for the emergence of quantum chaos as in the one-band Bose-Hubbard models studied in Refs. [28–30]. Yet, in our two-band model, $F$ can also be large, and the RET allows us to squeeze many-body energy levels in order to enforce a chaotic level structure. Hence, our new model allows us to switch between more or less regular and chaotic regimes in the vicinity of $F_r$ (see the manifold picture in Sec. III A and Fig. 3).

As a final remark, for our spectral analysis, we did not take into account those systems for which the greatest common divisor $\gcd(N, L)$ is larger or is equal to 1 due to the existence of a temporal symmetry of the Hamiltonian as reported in Ref. [28]. In the following, we discuss important consequences that emerge from the spectral properties studied so far for the many-body Wannier-Stark system defined by Eq. (1).

## IV. DIFFUSION IN HILBERT SPACE

### A. Eigenstate diffusion

The structure of avoided crossings presented above provides a perfect setup for studying dynamical processes generated by a cascade of single LZ events around $F_r$.

#### 1. Time evolution

We now focus on the diffusion process triggered by the parametric time evolution of different initial conditions with $F(t) = F_0 + \alpha t$ and with $\alpha = \Delta F/\Delta T$. In analogy to the LZ problem [42], we use a linear sweep. Here $\Delta F$ represents the effective extension of the RET regime, and $\Delta T$ is the time needed to evolve the initial state from a starting tilt $F_0$ to
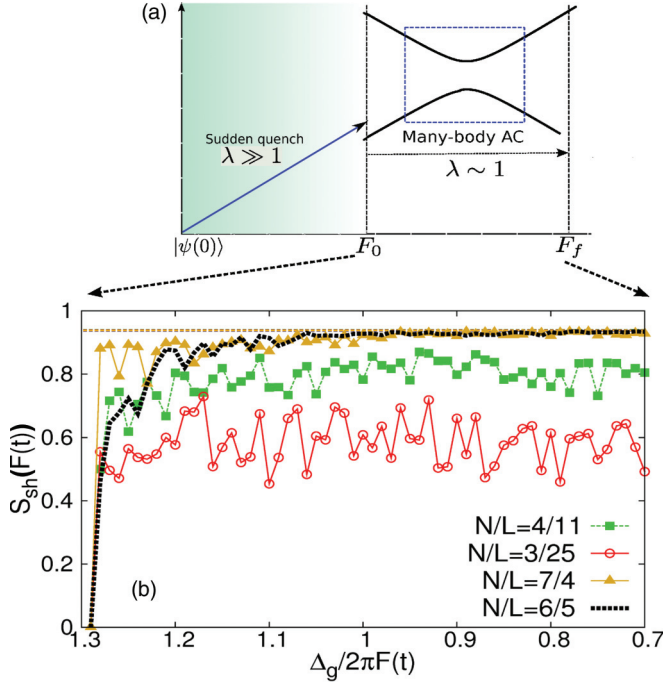
FIG. 5. (Color online) Diffusion: (a) Sketch of the sweeping process. The initial state $|\psi(0)\rangle$ is prepared at $F = 0$ and suddenly is evolved by means of a quench from $F = 0$ to $F = F_0$ ($\lambda \gg 1$). After this process, the state is then further evolved but nonadiabatically ($\lambda \sim 1$) from $F = F_0$ to $F = F_f$ across the many-body AC during a finite time $\Delta T$. The resonance order is $r = 1$ with $F_{r=1} = 0.045$. (b) Spreading of the evolved state $|\psi(t)\rangle$ measured by the Shannon entropy $S_{sh}$ when dynamically crossing the RET regime. The parameters are $\lambda = 0.7$, $\Delta_g = 0.285$, $J_a = 0.0382$, $J_b = -0.0417$, $W_a = 0.028$, $W_b = 0.029$, $W_x = 0.029$, $C_0 = -0.096$, $C_1 = 0.046$, and $C_2 = 0.008$.

the final one $F_f$ [see Fig. 5(a)], i.e., the sweeping time. A reasonable value for $\Delta T$ and, hence, for the sweeping rate $\alpha$, is given by the Heisenberg relation $\Delta T d \approx 1$, where $d \approx \Delta E/\mathcal{N}_s$ is the mean level spacing of the many-body spectrum at $F_r$. We now rewrite the Hamiltonian as follows:

$$\hat{H}(t) = \hat{H}_0 + \hat{J}^{\dagger}e^{-i2\pi F(t)t} + \sum_{\mu} \hat{C}_{\mu}^{\dagger}e^{-i2\pi\mu F(t)t} + \text{H.c.,} \quad (15)$$

with $\hat{H}_0$, $\hat{J}$, and $\hat{C}_{\mu}$ as defined in Sec. II B. We can study two types of dynamics using (15): first, by fixing the Stark force $F(t) = F$. This implies that the Hamiltonian is temporally periodic and fulfills all properties described in Sec. II A. The time evolution of the initial state $|\psi(0)\rangle$ is, thus, obtained through stroboscopic quantum maps $|\psi(m+1)T_B\rangle = \hat{U}_{T_B}|\psi(mT_B)\rangle$ with $m$ as an integer. Second, when considering the time-dependent pulse $F(t) = F_0 + \alpha t$, the periodicity is broken. The temporal evolution must then be explicitly computed, e.g., by using a fourth-order Runge-Kutta method. In addition, $\hat{H}(F(t))$ no longer preserves the time-reversal symmetry, therefore, the expansion coefficients of state $|\psi(t)\rangle$ in any basis are, in general, complex numbers.

To determine the parameter regime for the dynamical evolution, we define the parameter $\lambda \equiv \alpha/d\,\Delta F$. The diabatic passage (or sudden quench) is set by $\lambda \gg 1$. We expect an adiabatic evolution for $\lambda \ll 1$ and a nonadiabatic one for

$\lambda \sim 1$. Hereafter, we concentrate on the nonadiabatic regime when driving the system through a single resonance [see Fig. 5(a)]. Furthermore, we set the time scale to be the Bloch period defined by the tilt for the exact single-particle resonance $F_r$, that is, $T_B = 1/F_r$. The Bloch period is small when $F_r$ is large. Therefore, for practical implementations, it is useful to concentrate on the dynamics across a first-order resonance. In Sec. III C, we have already seen that the manifold mixing is enhanced because of the chaotic spectral properties of the RET regime for $N/L \sim 1$.

### 2. Initial condition

To study the emerging diffusion process in Hilbert space, we have two natural choices for the initial conditions: the Floquet eigenstates at any fixed force $|\varepsilon_i(F)\rangle$ and the translationally invariant Fock basis states $|\gamma\rangle$. The two sets of states map one to one onto each other with probability $\gtrsim 80\%$ in the off-resonant regime due to the presence of the $M$ manifolds. In this way, if we choose $|\gamma\rangle$ as the initial state, it is well localized in the energy space [see Fig. 2(c)]. In this sense, we have, without loss of generality, generic initial conditions [14,17]. If the initial state is a Floquet eigenstate at $F_0$, then it is, by definition, well localized in the instantaneous spectrum at $F_0$.

### 3. Protocol

(i) The initial state $|\psi(0)\rangle$ is chosen to be, for instance, a Fock state with a well-defined upper band occupation number $M$. This may be prepared in the flat lattice condition, i.e., at $F = 0$. (ii) Then we evolve $|\psi(0)\rangle$ by suddenly ($\lambda \gg 1$) ramping the lattice as: $F = 0 \rightarrow F = F_0$. This allows us to set a nonequilibrium scenario as sketched in Fig. 5(a). (iii) Next, state $|\psi(F_0)\rangle$ is nonadiabatically driven ($\lambda \sim 1$) across the many-body AC from $F = F_0$ to $F = F_f$. When the evolution starts at $F_0$, a fast coupling of the initial state with the local eigenstates is expected since the spectrum at $F_0$ is highly mixed. Yet, if the spectrum at $F_0$ is well described in terms of manifolds, $|\psi(F_0)\rangle$ mixes in a first instance with the eigenstate members of the same manifold via hopping transitions before it mixes states from other manifolds. This latter process gives rise to manifold mixing in time and, hence, the diffusion in energy space.

### B. Localization-delocalization transition

To quantify the diffusive processes across the ACs, we compute the probability amplitudes $C_i(t) \equiv \langle\varepsilon_i(F_k)|\psi(t)\rangle$, where $\{|\varepsilon_i(F_k)\rangle\}$ is the set of local Floquet eigenstates at the instantaneous tilt $F(t = \Delta T_k) = F_k$ with $\Delta T_k = T_k - T_0$. As a function of the local energy space, the distribution of the probabilities $|C_i(t)|^2$ can be represented in terms of the *local density of states* (LDOS) [18,43],

$$P_{\psi}(\varepsilon,t) = \sum_i |C_i(t)|^2\delta(\varepsilon - \varepsilon_i), \quad (16)$$

which allows for a visualization of the transit of state $|\psi(t)\rangle$ across the ACs. At $F_0$, $P_{\psi}(\varepsilon,T_0)$ is $\delta$ shaped (as indicated by the arrow in Fig. 6). As the tilt increases with the time, $P_{\psi}(\varepsilon,t)$ starts to delocalize due to the multiple LZ transitions induced by the cluster of avoided crossings. The diffusion
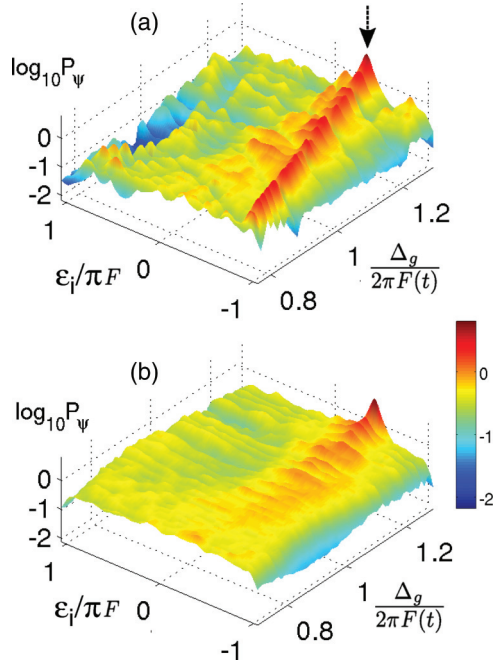
FIG. 6. (Color online) Diffusion: Temporal evolution of the initial state $|\psi(0)\rangle$ across the many-body AC represented by the local density of states $P_\psi(\varepsilon,t)$ as defined in Eq. (16). The panels show the respective transit through the energy spectra for (a) $N/L = 4/11$ and (b) $N/L = 6/5$. The remaining parameters are those of Fig. 5(b).

depends on $\alpha$ [11], but it is also highly sensitive to the type of statistical distribution of the spectrum in the vicinity of $F_r$. In Fig. 6(a), we show the evolution of $P_\psi(\varepsilon,t)$ corresponding to $N/L = 4/11$ with the initial state defined by a Floquet eigenstate with manifold number $M = [N/2]$ with $[\cdots]$ standing for the integer part. For this system, the spectrum at $F_r$ presents deviations of the full quantum chaotic regime as previously shown (see Fig. 4). The incoming state is well localized in energy space, and its localization is preserved with high probability after the passage through the RET regime, despite partial delocalization of $|\psi(t)\rangle$ around $F_r$. An initially localized state can stay well localized by two mechanisms: (i) by a fast diabatic driving across the many-level AC, similar to a diabatic crossing in a two-level Landau-Zener system; (ii) in the nonadiabatic dynamical regime, the instantaneous state can exchange its character ($M$) with the local eigenstates during the crossing through the RET domain. The outgoing state may be characterized either by the same manifold number $M$ [see Fig. 6(a)] or by a different one. This latter implies a change in the direction of the LDOS in the course of time in the plane $\varepsilon - F(t)$. The exchange of character is inherited from a two-level AC [8,10].

Localization properties of $P_\psi(\varepsilon,t)$ are analyzed by computing its second moment from which we obtain

$$\int \rho(\varepsilon) P_\psi^2(t) d\varepsilon = \sum_i |C_i(t)|^4 \equiv \xi_\psi(t). \quad (17)$$

$\xi_\psi(t)$ is the so-called inverse participation ratio, and $\rho(\varepsilon)$ is the density of states. In this way, the spreading over the local instantaneous spectrum can be quantitatively characterized by the average inverse participation ratio [43,44] and similarly by

the Shannon entropy [27], both defined as

$$\xi(F(t)) \equiv \left\langle \sum_{i=1}^{\mathcal{N}_s} |C_i(t)|^4 \right\rangle_\psi,$$

$$S_{\text{sh}}(F(t)) \equiv \left\langle -\sum_{i=1}^{\mathcal{N}_s} \frac{|C_i(t)|^2}{\log_{10}\mathcal{N}_s} \log_{10}|C_i(t)|^2 \right\rangle_\psi. \quad (18)$$

The average $\langle\cdot\rangle_\psi$ is taken over a large set of similar initial conditions $\{|\psi(0)\rangle\}$ with $M = [N/2]$. The measures in (18) depend on the choice of basis to compute the coefficients $C_i$. In the case of complete delocalization, the coefficients $\{|C_i|\}$ fluctuate around the equipartition condition $|C_i| = 1/\sqrt{\mathcal{N}_s}$. Therefore, the localization measures (16) converge to their respective minimal values, which can be computed under the assumption of complete randomness, i.e., no correlations between the coefficients. The set of coefficients $C_i$ satisfies a normalization condition $\sum_i |C_i(t)|^2 = 1$. Therefore, we have $(\mathcal{N}_s - 1)$-independent contributions. In the presence of chaos, the randomness of the above set of coefficients is guaranteed. Then by defining $y = |C_i|^2/\langle c^2 \rangle$ with $\langle c^2 \rangle$ being the average probability, the resulting distribution $f(y)$ follows a Porter-Thomas distribution [41]. Because the coefficients $C_i$ are, in general, complex numbers due to the breaking of time-reversal symmetry of (1) when considering $F(t)$, we must use the Gaussian unitary ensemble (GUE) [41]. For this ensemble, RMT predicts $f(y) = \exp(-y)$. Following Ref. [44] and using $f(y)$, we compute the GUE (or statistical) limits of the localization measures as

$$\xi = \mathcal{N}_s \langle c^2 \rangle^2 \int_0^\infty dy\, f(y) y^2, \quad (19)$$

$$S_{\text{sh}} = \mathcal{N}_s \int_0^\infty dy\, f(y) y \langle c^2 \rangle \ln(y \langle c^2 \rangle). \quad (20)$$

These integrals are accessible from which we obtain

$$\xi_{\text{GUE}} = \frac{2}{\mathcal{N}_s}, \qquad S_{\text{sh}}^{\text{GUE}} = 1 - \frac{\sigma_c}{\ln(\mathcal{N}_s)}, \quad (21)$$

with $\sigma_c = 0.422\,784$ [10]. We represented $S_{\text{sh}}^{\text{GUE}}$ by the horizontal dashed lines in Fig. 5(b) along with the Shannon entropy $S_{\text{sh}}(F(t))$ for different filling factors.

In the case of deviations from the chaotic level spacing distributions ($N/L = 3/25,4/11$), the time-evolved state never reaches the GUE limits but remains localized instead [see Fig. 5(b)]. The maximization of the entropy implies a dynamical equilibrium [18,20]. Under this condition, the density operator $\hat{\rho}(t) = |\psi(t)\rangle\langle\psi(t)|$ diagonalizes in the local energy basis. We, thus, get $\langle\varepsilon_i|\hat{\rho}(t)|\varepsilon_j\rangle \approx |C_i|^2\delta_{i,j}$ since the off-diagonal terms drop to zero. Then the Shannon and von Neumann entropies coincide [19]. At this point, it is easily noticed that, under chaotic conditions, the density operator also diagonalizes in the Fock basis. This implies no further (re)localization in the course of the evolution, hence, strong mixing of the complete set of manifolds is obtained.

### C. Spectral ergodicity and relaxation toward equilibrium

Previously, we have seen that, in the course of the time evolution, the system undergoes a dynamical diffusion [see Fig. 5(b)] in the accessible Hilbert space. This diffusive

spreading is much stronger for chaotic spectra ($N/L = 6/5, 7/4$) than for Poissonian or mixed ones ($N/L = 3/25, 4/11$). The latter manifests itself in a (re)localization during the passage through the RET regime. The LDOS, locally in energy space, is, thus, described by the *Breit-Wigner* formula [45],

$$P_\psi(\varepsilon, t) \sim \frac{1}{\pi} \frac{\Gamma^2/4}{(\varepsilon - \varepsilon_0)^2 + \Gamma^2/4}, \qquad (22)$$

where $\Gamma$ is the width of the distribution and $\varepsilon_0$ is its mean position in the spectrum. In the fully quantum chaotic (Wigner-Dyson-distributed) case, such a (re)localization does not take place as shown in Fig. 5(b) for $N/L \gtrsim 1$. $P_\psi(\varepsilon, t)$ is then a uniform function over the entire FZ. In this way, we see that the system undergoes spectral ergodicity in the course of the evolution since the equipartition condition $|C_i(t)|^2 \approx 1/\mathcal{N}_s$ is fulfilled.

The presence of chaos also plays an important role in the evolution at the fixed force of an initial condition after a quench $F: 0 \to F_r$. This latter is straightforwardly shown by computing the long-time average of the basis projector $\hat{P}_\gamma \equiv |\gamma\rangle\langle\gamma|$, i.e.,

$$\overline{\langle\psi(t)|\hat{P}_\gamma|\psi(t)\rangle} = \lim_{\tau\to\infty} \frac{1}{\tau} \int_0^\tau dt \langle\psi(t)|\hat{P}_\gamma|\psi(t)\rangle. \qquad (23)$$

To compute the above average, we can use the evolution operator of the Floquet formalism given in Ref. [46],

$$\hat{U}(t_2, t_1) = \sum_{j, k_1, k_2} e^{-i\varepsilon_j(t_2 - t_1)} e^{i\omega_B k_1 t_1} e^{-i\omega_B k_2 t_2} |\phi_{\varepsilon_j}^{k_2}\rangle\langle\phi_{\varepsilon_j}^{k_1}|. \qquad (24)$$

Choosing the initial state to be, for example, the state $|\psi(0)\rangle = |\gamma\rangle$ and assuming nondegeneracies of the Floquet eigenenergies, one finds

$$\bar{P}_\gamma(F_r; |\gamma\rangle) \approx \xi_\gamma = \sum_j p_j^\gamma \langle\varepsilon_j|\hat{P}_\gamma|\varepsilon_j\rangle, \qquad (25)$$

where $\xi_\gamma = \sum_j |\langle\gamma|\varepsilon_j(F_r)\rangle|^4$ and the right-hand term is just the spectral average of the projector $\hat{P}_\gamma$ [10]. Here the occupation probabilities satisfy the normalization condition $\sum_j p_j^\gamma = 1$. The strong mixing properties of the spectrum, which give rise to quantum chaos, are, thus, also responsible for two dynamical processes: diffusion and relaxation of the system initially prepared in $|\psi(0)\rangle$, either by sweeping across the spectrum ($F(t) \sim \alpha t$) or by the dynamical evolution after the quench to a fixed tilt $F = F_r$. Note that $\bar{P}_\gamma(F_r; |\gamma\rangle)$ is nothing else but the long-time average of the survival probability for the initial state $|\psi(0)\rangle = |\gamma\rangle$.

A basic feature of chaos is that all possible dynamical processes take place with the same probability. The result is a mixture of all different time scales in the evolution. For a system started at $F_0$ very far away from $F_r$, the only possible transitions are intramanifold ones, which occur due to the hopping transitions, i.e., by $J_\beta$ in Eq. (2). In this process, for a given initial state $|\gamma\rangle$, one expects that its survival probability $\bar{P}_\gamma$ showed collapses but also some revivals before $F_r$. Once the mixing between neighbor manifolds takes place, the system diffuses, and this effect is very much enhanced when crossing the AC structure. One way to characterize the manifold mixing

is by defining the degree-of-mixing parameter,

$$\zeta(t) = 1 - \sum_M [p_M(t)]^2, \qquad p_M(t) = \langle\psi(t)|\hat{P}_M|\psi(t)\rangle, \qquad (26)$$

with $\hat{P}_M$ as defined in Sec. II A. Clearly, in the case of a fully chaotic RET domain, no revivals are observed, therefore, maximal manifold mixing arises. $\zeta(t)$ is, thus, maximized, and its maximal value is given by $\zeta_{\max} \approx 1 - 1/N$ with $N$ as the total particle number. The system is subjected to a dynamical relaxation process, which is characterized by a power-law (scale-free) decay of the localization measures. To see this, we look at the time-average function defined as

$$T\text{-averaged } h(t) = \frac{1}{\Delta T_k} \sum_{t=0}^{\Delta T_k} h(t), \qquad (27)$$

where $h(t)$ is either the inverse participation ratio or the Shannon entropy.

In Fig. 7(a), we show a double-logarithmic plot of the time evolution of the inverse participation ratio. Two different power laws are observed (see straight lines). In a first instance, the full chaotic spectra $N/L = 6/5, 7/4$ show a well-defined decay $t^{-\nu}$ with exponents $\nu \approx 0.78$ before $F_r$ (indicated by the arrows). Afterwards, a slowing down for $F > F_r$ occurs due to the maximization of the spreading in the instantaneous eigenbasis. The exponent for this region is $\nu \approx 0.5$. In the latter case, the straight lines depict the tendency of the evolution if $\Delta T$ is extended to again reach the off-resonant regime where the mixing is suppressed. In this regime, the equidistribution of the probability over the energy space remains unchanged, explaining the slowing down in Fig. 7.
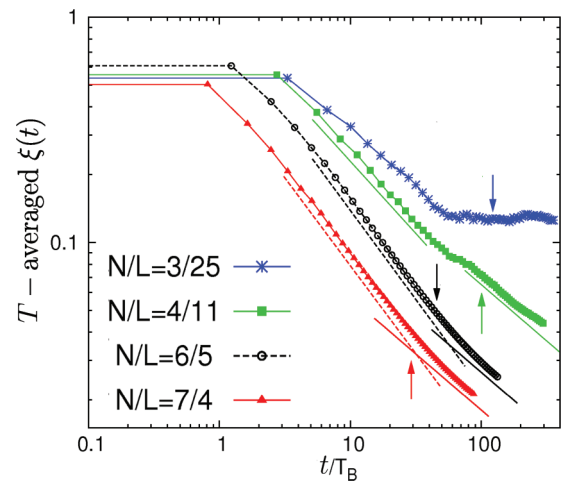


FIG. 7. (Color online) Relaxation: time-averaged inverse participation ratio $\xi$ for $N/L = 4/11$, $6/5$, and $7/4$. The straight lines indicate the power-law tendency of the diffusion processes with $t^{-0.78}$ for chaotic spectra before the resonance $F_{r=1}$ and $t^{-0.5}$ for $F > F_r$. The change in the exponents corresponds to a slowing down of the spreading of the evolved state since, in the chaotic case, the maximal delocalization has already occurred. For the not fully chaotic spectra $N/L = 4/11$, the tendency to a power law $t^{-0.64}$ is destroyed by the emerging relocalization as explained in Sec. IV B, see cf. $N/L = 3/25$.

For $N/L = 3/25, 4/11$, deviations from chaotic spectra occur (see Sec. III C). Here the time-evolved states undergo different processes in the course of the evolution. We observe a tendency to a power law with $\nu \approx 0.64$ ($N/L = 4/11$), but also a slowing down before $F_r$, interestingly, right before $F_r$ localization occurs. After $F_r$, the short-time decay also presents a power-law exponent $\nu \approx 0.5$, which implies a certain stabilization (slowing down). Yet for long times, one observes final relocalization highlighted by a second slowing down. This is most clearly seen for $N/L = 3/25$ where the decay stops completely [see asterisks in Fig. 7]. It does, however, not undergo any equilibration. We see that chaos, apart from generating strong band mixing, also induces a fast decay to the equilibrium values set by the GUE limits of Eq. (21). In Fig. 7, one can also notice that the system diffuses the slower, the smaller the filling factor $N/L$.

In our case, the equilibrium is defined in the context of the energy shell approach [18]. However, the connection is not straightforward since, in our case, the distribution of coefficients $C_i$ as a function of the energies within the Floquet zone is nearly a flat function. Therefore, the LDOS is an extended function over the entire spectrum. In the energy shell approach, the distribution of the coefficients is expected to be Gaussian distributed. To solve such a discrepancy, one must perform an unfolding of the distribution $P_\psi$, or equivalently, one can fold the Gaussian profile into the FZ. The latter method is straightforward since the resulting function is a *normal*

*wrapped distribution* [47], which is a periodic function in the energy domain, meaning, in our case, in the FZ zone.

As final result, we show the dynamical creation and destruction of the $M$ manifolds. This is performed by computing the manifold mixing degree $\zeta(\Delta T)$ (or the localization measures) and the manifold number $M(\Delta T)$ at the final time, i.e., at $F_f > F_r$. The results are shown in Fig. 8 for (a) $N/L = 4/11$ and (b) $N/L = 6/5$. For this calculation, we have evolved more than $\mathcal{N}_s/2$ different initial conditions belonging to all possible sets of manifolds. Some of them are plotted in Fig. 8(c), which shows the trajectories in the plane $\zeta$-$M$. One must keep in mind that the number of manifolds is $N + 1$. Taking the final time $\Delta T$ as a parameter, panels (a) and (b) show the destruction of the manifolds as the gap decreases below a critical value of $\Delta_g \approx 0.285$. Here one can no longer identify the separated bunches of states with well-defined manifold numbers. The latter dynamical effect is expected according to the discussion in Sec. II A. In addition, the mixing does not depend on the class of initial states. For the fully chaotic spectrum $\Delta_g = 0.155$, all final states are completely delocalized. This implies that $M = N/2$ and $\zeta(\Delta T) \approx 1 - 1/N$ as around (26), dashed lines in Figs. 8(a) and 8(b), which is exactly the equilibrium condition. We, thus, confirm that the outgoing state, after the passage across the RET is, indeed, an equilibrium state for which the respective entropy is maximized due to the presence of the fully chaotic many-body AC structure.

## V. CONCLUSIONS

We have studied, in detail, the spectral properties of a many-body two-band Wannier-Stark system with particular emphasis on the resonant tunneling regime. Depending on the strength of the interaction on the band gap between the two lowest energy bands and on the filling factor, the spectra show a regular to quantum-chaotic transition. This allows us to study the diffusive properties of generic energy spectra in Hilbert space. The spectral characteristics can be probed by quantum sweeps of different initial conditions across the resonant regions by using the Stark force as a time-dependent control parameter. In this way, we can clearly distinguish the dynamics depending on the various spectral characteristics. Relaxation toward equilibrium, corresponding to a maximal delocalization in energy (Hilbert) space occurs for quantum chaotic spectra. Interestingly, the spectral ergodicity arises in both types of dynamics, either by sweeping across the chaotic many-body RET regime, or by a quench with additional free evolution at fixed tilt.

In the case of regular or mixed spectra, showing a Poissonian component in the nearest-neighbor statistics, localization of the instantaneous states preserves in the dynamics. In this case, full ergodicity cannot arise. The manifold approach developed here, starting from the single-particle (noninteracting) case, has proved to be a good tool for analyzing the localization-delocalization transition. It provides an intuitive picture based on the mixing of the manifolds during the temporal evolution. The transition between the various regimes can be controlled by means of the system parameters, in particular, the interparticle interaction, the filling factor, and the Stark force.
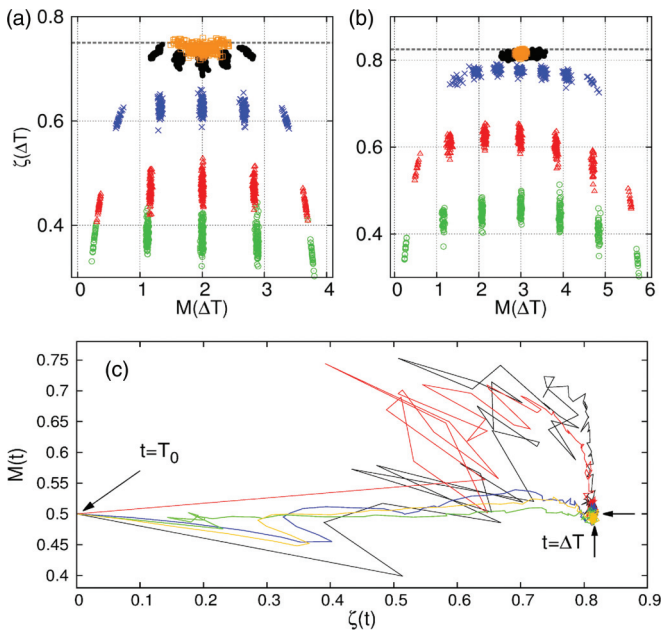


FIG. 8. (Color online) Manifold mixing: (a) and (b) depict the final time-manifold degree of mixing $\zeta(\Delta T)$ and manifold creation $M(\Delta T)$ for different band gaps: $\Delta_g = 2.53$ (green $\circ$), $\Delta_g = 1.16$ (red $\triangle$), $\Delta_g = 0.556$ (blue $\times$), $\Delta_g = 0.285$ (black $\bullet$), and $\Delta_g = 0.155$ (dark orange $\square$). To this end, more than $\mathcal{N}_s/2$ initial states were evolved starting at $F_0 = 0$ for (a) $N/L = 4/11$ and (b) $N/L = 6/5$. Panel (c) depicts $\zeta(t)$ vs $M(t)$ with $t$ as a parameter for $\Delta_g = 0.155$. Note that all trajectories in the plane $\zeta$-$M$ converge to the equilibrium point ($\zeta_{\max}, M = N/2$) (see the main text).

As explained in the Appendix, our two-band system can readily be realized in the experiment. Its implementation is based on the miniband structure, which can easily be engineered using a double period one-dimensional lattice [48,49]. A standard procedure for controlling, i.e., the Stark force, is by accelerating the lattice structure by shifting the frequencies of two counterpropagating waves that generate the optical potential [8,24,48,50]. Our system offers a high controllability of all system parameters. For instance, the interparticle interaction ($g \sim a_{\text{scatt}}$) can be changed by Feshbach resonances [2,7]. The remaining parameters can be varied by using the geometry properties of the lattice. Observing the single-band populations [8,24,33], in principle, also with single-site resolution [6,51], signatures of the here-discussed spectral diffusion and equilibration could be experimentally investigated.

In this way, our engineered system and results exposed in this paper open an interesting route toward the realization of complex many-body systems with immediate experimental implications on coherent control of ultracold atoms [5–9,52].

## ACKNOWLEDGMENTS

## APPENDIX: WANNIER FUNCTIONS AND BOSE-HUBBARD COEFFICIENTS

Here we show how the coefficients in Eq. (2) are computed for an experimental realization with ultracold bosons in an optical lattice. We based our calculation on the single-particle Wannier functions, which are localized within each site. We suggest using a double periodic optical lattice as experimentally realized in Refs. [48,49],

$$V(x) = -V_0[\cos(2k_L x) + z_0 \cos(4k_L x + \phi)], \quad \text{(A1)}$$

with $k_L$ being the recoil momentum and the recoil energy $E_r = \hbar^2 k_L^2 / 2m_0$. The energy dispersion relation is computed by diagonalizing the Hamiltonian $\hat{H}_0 = \hat{p}^2/2m_0 + V(x)$ as a function of the lattice parameters: the depth $V_0$ of the lattice, the ratio $z_0 = V_1/V_0$ between the amplitudes of the two lattices, and the phase difference $\phi$. One can, thus, appropriately engineer a periodic potential for which the respective two lowest Bloch bands are well separated from all higher-energy bands [48] as shown in Fig. 9. In this way, by choosing a relative phase $\phi \equiv \pi$ and appropriate values of $z_0$, we can work with a realistic closed two-band model, represented by our Hamiltonian in Eq. (1). The Wannier functions are defined through the Fourier transform of the Bloch functions $\psi_{\beta,\tilde{k}}(x) = e^{i\tilde{k}x} u_\beta(x)$ in the first Brillouin zone (BZ) as

$$\chi_\beta(x) = \int_{BZ} e^{-i\tilde{k}x_l} \psi_{\tilde{k}}^\beta(x) d\tilde{k}, \quad \text{(A2)}$$
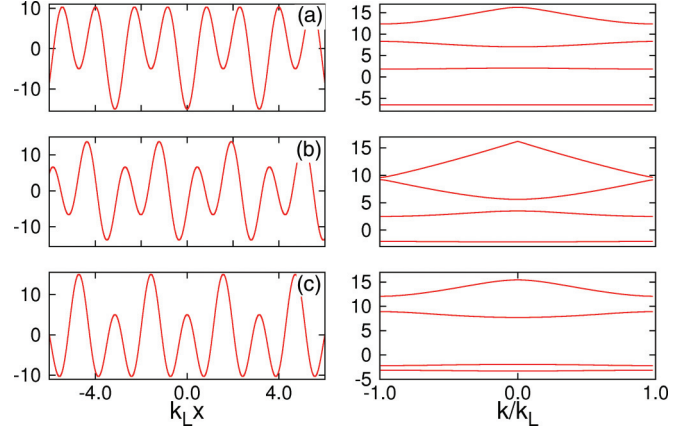


FIG. 9. (Color online) Profile of the optical lattice (left) and its respective band structure (right) for $V_0 = 3$ and $z_0 = 4$ as a function of the phase difference $\phi$. (a) $\phi = 0$, (b) $\phi = \pi/2$, and (c) $\phi = \pi$.

with $u_\beta(x) = u_\beta(x + d_L)$. $d_L$ is the spatial periodicity of the lattice, and $x_l \to d_L l$. Since $\tilde{k} = k/k_L$ is a parameter, the Bloch functions are not unique, and a phase factor can be chosen such that the Wannier functions are highly localized [25,30,53]. The latter property and the appropriate symmetry $\chi_\beta(-x) = (-1)^{\beta-1} \chi_\beta(x)$ are shown to be satisfied by the following functions:

$$\chi_1(x) = \frac{1}{\sqrt{N_1}} \sum_{k_{j,n}} |u_n(1,\tilde{k}_j)| \cos[k_{j,n} x_0] \cos[k_{j,n} x],$$

$$\chi_2(x) = \frac{i}{\sqrt{N_2}} \sum_{k_{j,n}} |u_n(2,\tilde{k}_j)| \sin[k_{j,n} x_0] \sin[k_{j,n} x], \quad \text{(A3)}$$

where $k_{j,n} \equiv 2n + \tilde{k}_j$. $x_0 = \pm \cos^{-1}(1/4z_0)$ are the first minima positions of the potential in Eq. (A1) around $x = 0$, and $N_{1,2}$ are normalization constants. The coefficients $u_n(\beta, \tilde{k}_j)$ are the Fourier components of the periodic function $u_\beta(x)$ given by $u_\beta(x) = \sum_n u_n(\beta, \tilde{k}) e^{-inx}$.

The Bose-Hubbard coefficients, sketched in Fig. 10(a), are then obtained from the following relations: The hopping amplitudes $J_\beta$ are

$$J_{l-l'}^\beta \equiv \int \chi_\beta^*(x - x_l) H_0(x) \chi_\beta(x - x_{l'}) dx = \epsilon_{l-l'}^\beta, \quad \text{(A4)}$$

where $J_a \equiv J_1^{\beta=a}$, $J_b \equiv J_1^{\beta=b}$, and $\Delta_g = |\epsilon^b - \epsilon^a| = |J_0^{\beta=b} - J_0^{\beta=a}|$. The dipolelike coupling strengths are

$$C_{l-l'}^{\beta\beta'} \equiv \int \chi_\beta^*(x - x_l) x \chi_{\beta'}(x - x_{l'}) dx, \quad \text{(A5)}$$
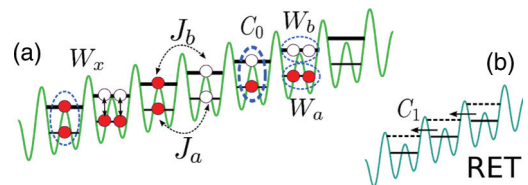


FIG. 10. (Color online) : (a) Many-body processes of the two-band Bose-Hubbard Hamiltonian for a bichromatic tilted optical lattice. (b) RET condition for the nearest-neighboring double wells, i.e, for a first-order resonance.

with $C_\mu \equiv C_\mu^{ab}$. Because of the high localization of the Wannier functions, coefficients with $|\mu| > 0$ are at least one order of magnitude smaller than $C_0$. Thus, we only take into account the strength with $|\mu| = 0$, 1, and 2 for the first two resonances $r = 1,2$. Finally, the repulsive intraband on-site interparticle interaction terms are given by

$$W_\beta \equiv g_{1D} \int |\chi_\beta(x)|^4 dx. \qquad (A6)$$

The interband on-site interparticle interaction is

$$W_x \equiv g_{1D} \int |\chi_a(x)|^2 |\chi_b(x)|^2 dx, \qquad (A7)$$

where the interaction strength is defined by $g_{1D} = 4\pi a_{1D}/m_0$ with $a_{1D}$ as the one-dimensional scattering constant and $m_0$ as the mass of the atoms [2].

---

[1] M. Lewenstein, A. Sanpera, V. Ahufinger, B. Damski, A. Sen De, and U. Sen, Adv. Phys. **56**, 243 (2007).

[2] I. Bloch, J. Dalibard, and W. Zwerger, Rev. Mod. Phys. **80**, 885 (2008).

[3] C. Weitenberg, M. Endres, J. F. Sherson, M. Cheneau, P. Schauß, T. Fukuhara, I. Bloch, and S. Kuhr, Nature (London) **471**, 319 (2011).

[4] M. Köhl, H. Moritz, T. Stöferle, K. Günter, and T. Esslinger, Phys. Rev. Lett. **94**, 080403 (2005); G. Wirth, M. Ölschläger, and A. Hemmerich, Nat. Phys. **7**, 147 (2010); M. Ölschläger, G. Wirth, T. Kock, and A. Hemmerich, Phys. Rev. Lett. **108**, 075302 (2012).

[5] T. Müller, S. Fölling, A. Widera, and I. Bloch, Phys. Rev. Lett. **99**, 200405 (2007).

[6] J. Simon, S. Bakr, M. Ruichao, M. E. Tai, M. Preiss, and M. Greiner, Nature (London) **472**, 307 (2011); W. S. Bakr, P. M. Preiss, M. E. Tai, Ruichao Ma, J. Simon, and M. Greiner, ibid. **480**, 500 (2011).

[7] F. Meinert, M. J. Mark, E. Kirilov, K. Lauber, P. Weinmann, A. J. Daley, and H.-C. Nägerl, Phys. Rev. Lett. **111**, 053003 (2013).

[8] M. G. Bason, M. Viteau, N. Malossi, P. Huillery, E. Arimondo, D. Ciampini, R. Fazio, V. Giovannetti, R. Mannella, and O. Morsch, Nat. Phys. **8**, 147 (2011); N. Malossi, M. G. Bason, M. Viteau, E. Arimondo, R. Mannella, O. Morsch, and D. Ciampini, Phys. Rev. A **87**, 012116 (2013).

[9] J. P. Ronzheimer, M. Schreiber, S. Braun, S. S. Hodgman, S. Langer, I. P. McCulloch, F. Heidrich-Meisner, I. Bloch, and U. Schneider, Phys. Rev. Lett. **110**, 205301 (2013).

[10] C. A. Parra-Murillo, Ph.D. thesis, Heidelberg University, 2013.

[11] M. Wilkinson, J. Phys. A **21**, 4021 (1988); Phys. Rev. A **41**, 4645 (1990).

[12] L. D'Alessio and A. Polkovnikov, Ann. Phys. (NY) **333**, 19 (2013).

[13] C. Kasztelan, S. Trotzky, Y.-A. Chen, I. Bloch, I. P. McCulloch, U. Schollwöck, and G. Orso, Phys. Rev. Lett. **106**, 155302 (2011); S. Trotzky, Y-A. Chen, A. Flesch, I. P. McCulloch, U. Schollwöck, J. Eisert, and I. Bloch, Nat. Phys. **8**, 325 (2012).

[14] J. M. Deutsch, Phys. Rev. A **43**, 2046 (1991).

[15] M. Srednicki, Phys. Rev. E **50**, 888 (1994).

[16] A. Altland and F. Haake, Phys. Rev. Lett. **108**, 073601 (2012).

[17] M. Rigol and M. Srednicki, Phys. Rev. Lett. **108**, 110601 (2012); L. F. Santos and M. Rigol, Phys. Rev. E **81**, 036206 (2010).

[18] L. F. Santos, F. Borgonovi, and F. M. Izrailev, Phys. Rev. Lett. **108**, 094102 (2012); Phys. Rev. E **85**, 036209 (2012).

[19] A. Polkovnikov, Ann. Phys. (NY) **326**, 486 (2011).

[20] C. Gogolin, M. P. Müller, and J. Eisert, Phys. Rev. Lett. **106**, 040401 (2011).

[21] O. Morsch and M. Oberthaler, Rev. Mod. Phys. **78**, 179 (2006).

[22] E. Arimondo and S. Wimberger, in Dynamical Tunneling, edited by S. Keshavamurthy and P. Schlagheck (Taylor & Francis/CRC, Boca Raton, FL, 2011).

[23] E. Arimondo, D. Ciampini, A. Eckardt, M. Holthaus, and O. Morsch, Adv. At., Mol., Opt. Phys. **61**, 515 (2012).

[24] C. Sias, A. Zenesini, H. Lignier, S. Wimberger, D. Ciampini, O. Morsch, and E. Arimondo, Phys. Rev. Lett. **98**, 120403 (2007); A. Zenesini, H. Lignier, G. Tayebirad, J. Radogostowicz, D. Ciampini, R. Mannella, S. Wimberger, O. Morsch, and E. Arimondo, ibid. **103**, 090403 (2009).

[25] M. Glück, A. R. Kolovsky, and H. J. Korsch, Phys. Rep. **366**, 103 (2002).

[26] R. Messina, S. Pelisson, M.-C. Angonin, and P. Wolf, Phys. Rev. A **83**, 052111 (2011).

[27] A. R. Kolovsky and A. Buchleitner, Europhys. Lett. **68**, 632 (2004).

[28] A. R. Kolovsky and A. Buchleitner, Phys. Rev. E **68**, 056213 (2003).

[29] A. Tomadin, R. Mannella, and S. Wimberger, Phys. Rev. Lett. **98**, 130402 (2007).

[30] A. Tomadin, R. Mannella, and S. Wimberger, Phys. Rev. A **77**, 013606 (2008).

[31] P. Buonsante and S. Wimberger, Phys. Rev. A **77**, 041606(R) (2008).

[32] J. E. Avron, Ann. Phys. **143**, 33 (1982).

[33] A. Zenesini, C. Sias, H. Lignier, Y. Singh, D. Ciampini, O. Morsch, R. Mannella, E. Arimondo, A. Tomadin, and S. Wimberger, New J. Phys. **10**, 053038 (2008).

[34] P. Plötz, J. Madroñero, and S. Wimberger, J. Phys. B **43**, 081001 (2010).

[35] P. Plötz, P. Schlagheck, and S. Wimberger, Eur. Phys. J. D **63**, 47 (2011).

[36] Y.-A. Chen, S. D. Hubber, S. Trotzky, I. Bloch, and E. Altman, Nat. Phys. **7**, 61 (2010).

[37] J. H. Shirley, Phys. Rev. **138**, B979 (1965); Y. B. Zeldovich, Sov. Phys. JETP **24**, 1006 (1967).

[38] T.-S. Ho and Shih-I. Chu, Phys. Rev. A **31**, 659 (1985).

[39] C. Lanczos, J. Res. Natl. Bur. Stand. **45**, 225 (1950).

[40] F. M. Izrailev, Phys. Scr., T **90**, 95 (2001).

[41] F. Haake, Quantum Signatures of Chaos (Springer, Heidelberg, 2001).

[42] L. D. Landau, Phys. Z. Sowjetunion **2**, 46 (1932); C. Zener, Proc. R. Soc. London, Ser. A **137**, 696 (1932); E. C. G. Stückelberg,

Helv. Phys. Acta **5**, 369 (1932); E. Majorana, Nuovo Cimento **9**, 43 (1932).

[43] T. Dittrich and U. Smilansky, Nonlinearity **4**, 59 (1991).

[44] See Sec. 4.2 in V. Zelevinsky, B. A. Brown, N. Fraziera, and M. Horoia, Phys. Rep. **276**, 85 (1996).

[45] G. Breit and E. Wigner, Phys. Rev. **49**, 519 (1936); M. Klein, D. Robert, and X. P. Wang, Commun. Math. Phys. **131**, 109 (1990).

[46] A. Buchleitner, D. Delande, and J. C. Gay, J. Opt. Soc. Am. B **12**, 505 (1995); A. Krug, Ph.D. thesis, LMU, Munich, 2001.

[47] F. I. Fisher, *Statistical Analysis of Circular Data* (Cambridge University Press, Cambridge, UK, 1996); see also Sec. 3.2 in S. Wimberger, I. Guarneri, and S. Fishman, Nonlinearity **16**, 1381 (2003).

[48] T. Salger, C. Geckeler, S. Kling, and M. Weitz, Phys. Rev. Lett. **99**, 190405 (2007).

[49] G. Roati, C. D'Errico, L. Fallani, M. Fattori, C. Ford, M. Zaccanti, G. Modugno, M. Modugno, and M. Inguscio, Nature (London) **453**, 895 (2008); E. Lucioni, B. Deissler, L. Tanzi, G. Roati, M. Zaccanti, M. Modugno, M. Larcher, F. Dalfovo, M. Inguscio, and G. Modugno, Phys. Rev. Lett. **106**, 230403 (2011).

[50] M. B. Dahan, E. Peik, J. Reichel, Y. Castin, and C. Salomon, Phys. Rev. Lett. **76**, 4508 (1996); S. R. Wilkinson, C. F. Bharucha, K. W. Madison, Q. Niu, and M. G. Raizen, *ibid.* **76**, 4512 (1996).

[51] W. S. Bakr, J. I. Gillen, A. Peng, S. Fölling, and M. Greiner, Nature (London) **462**, 74 (2009); J. F. Sherson, C. Weitenberg, M. Endres, M. Cheneau, I. Bloch, and S. Kuhr, *ibid.* **467**, 68 (2010); J. H. Lee, E. Montano, I. H. Deutsch, and P. S. Jessen, Nat. Commun. **4**, 2027 (2013); E. A. Salim, S. C. Caliga, J. B. Pfeiffer, and D. Z. Anderson, Appl. Phys. Lett. **102**, 084104 (2013).

[52] R. Ma, M. E. Tai, P. M. Preiss, W. S. Bakr, J. Simon, and M. Greiner, Phys. Rev. Lett. **107**, 095301 (2011).

[53] W. Kohn, Phys. Rev. B **7**, 4388 (1973); G. H. Wannier, Phys. Rev. **117**, 432 (1960).